Estimating Extreme Gusts via Optical Flow Tracking from Defoliated Tree Motion

Sai Kulkarni[1], John K. Hillier[1], Sarah L. Bugby[2], Tim I. Marjoribanks[3], Daniel Bannister[4], Jonny Higham[5], Rufus Dickinson[3], Matthew C. Baddock[1]

[1]Department of Geography and Environment, Loughborough University, Loughborough, LE11 3TU, UK
[2]Department of Physics, Loughborough University, Loughborough, LE11 3TU, UK
[3]School of Architecture, Building and Civil Engineering, Loughborough University, Loughborough, LE11 3TU, UK
[4]Willis Research Network, WTW, London, UK
[5]Department of Geography and Planning, University of Liverpool, Liverpool L69 7ZT, UK

Keywords: Extreme Wind Gusts, Visual Anemometry, Optical Flow Tracking Velocimetry (OFTV), Defoliated Tree Motion Simulation

Declaration of competing interest

The authors declare that they have no known competing interests that could have appeared to influence the work reported in this paper.

Funding

This work was supported and funded by Loughborough University and Willis Research Network, WTW. Any opinions, findings, and conclusions or recommendations expressed in this material are those of the author(s) and do not necessarily reflect the views of Loughborough University or WTW.

Author Contributions

Sai Kulkarni: Writing - original draft, Writing - review & editing, Data acquisition, Methodology, Visualisation, Formal analysis, Data curation, Conceptualisation. John Hillier: Writing -review & editing, Supervision, Methodology, Funding acquisition, Conceptualisation. Tim Marjoribanks: Writing - review & editing, Supervision, Methodology, Conceptualisation. Sarah Bugby: Writing -review & editing, Supervision, Methodology, Conceptualisation. Daniel Bannister: Writing- review & editing, Methodology, Conceptualisation. Jonny Higham: Software, Writing - review & editing, Supervision, Methodology. Rufus Dickinson: Data acquisition, Methodology, Writing -review & editing. Matthew Baddock: Data acquisition, Writing- review & editing, Methodology

Acknowledgements

We thank Dr Scott Van Pelt (United States Department of Agriculture-Agricultural Research Service, Big Spring, Texas, USA) for assistance in gathering the wind dataset used as the input wind forcing for the simulations presented in this study.

Data availability statement

The dataset (videos, processed optical flow tracking velocity data, kinematic data and input wind files) supporting the findings of this study is available on https://doi.org/10.5281/zenodo.22124275.

Abstract

Peak 3-second gusts (s_3) during severe storms are critical drivers of wind damage, yet their fine-scale dynamics remain difficult to measure. Visual Anemometry (VA) unlocks the possibility of spatially dense wind speed estimates, yet its performance under extreme winds remains poorly understood. Here, we combine physics-based simulations of tree motion with Optical Flow Tracking Velocimetry (OFTV), allowing a first assessment of s_3 estimation for winds of 25-144 km/h across camera angles of 0-180°. Modelled tree velocities increased approximately linearly with input wind speed and were captured well by OFTV ($R^2 \approx 0.9$, $p < 0.05$), mechanistically demonstrating the validity of VA for extreme winds and structural loading. Against expectations, both predictive performance and the relationship between video motions and estimated s_3 are not significantly affected by camera angle (0°-180°), importantly indicating that multi-branch tree motion produces an angularly isotropic response. Moreover, directional effects reduce, becoming negligible, under strong winds. Demonstrating the robustness of tree-based VA for extreme wind gusts (e.g. no direction-dependent calibration needed) is a foundational step towards enhanced gust detection, hazard mapping, and risk assessment for planning and insurance.

1. Introduction

Peak 3-second gusts (s_3) govern many wind-related damage processes, as they represent short-duration extremes produced by turbulent airflow interactions with buildings and vegetation (Holmes et al. 2014; Lombardo 2021; Ren et al. 2025). Capturing these gusts at the spatial scales relevant for impact assessment remains challenging. Conventional measurement techniques, including in situ anemometry and remote sensing, provide accurate observations only at coarse spatial resolutions (Stull 1988; Suomi and Vihma 2018), leaving small-scale variations in ground-level extreme gusts unresolved. This limitation creates challenges for applications, including windstorm risk assessment and forecasting (e.g., early warning systems for extreme winds) (Klawa and Ulbrich 2003), damage estimation for insurance and disaster response (Cusack 2023; ECMWF), urban microclimate modelling and real-time hazard mapping (Roberts et al. 2014; Tan and Fang 2018).

Recent advances in visual anemometry (VA) have shown that wind-induced motion of objects in videos can be exploited to infer local wind conditions (e.g., Cardona et al. 2019), offering a modern pathway to traditional wind measures such as the Beaufort scale (Met Office 2023). Within the broader framework of VA, image-based approaches have been used to infer wind speeds from object motion, including particle image velocimetry (Dabiri et al. 2023), feature displacement tracking (Cardona et al. 2021; Cardona and Dabiri 2022; Zhou et al. 2023), optical flow emulator methods (Zhang et al. 2022), and machine-learning techniques (Cardona et al. 2019; Runia et al. 2020). Building on these, Kulkarni et al. (2026) presented a proof-of-concept using Optical Flow Tracking Velocimetry (OFTV) to extract

s_3 directly from videos of trees in a natural domestic setting. Whilst they found moderate correlations ($R^2 = 0.65$, $p < 0.05$) against ground-truth cup-anemometer measurements, this is likely due to limitations in how the anemometer converts cup rotation into wind speed, as they showed that OFTV-s_3 estimates are robust across different objects in the scene (flags, tree parts, grass, the anemometer cups), with correlations exceeding $R^2 \geq 0.92$. However, this previous study was limited to a low wind speed range (≤ 6 m/s), only conducted on two foliated trees and remains untested for different viewing angles and wind directions, which could potentially influence OFTV estimates.

To date, VA studies involving trees have been conducted exclusively on fully foliated specimens. In such trees, the large leaf area increases aerodynamic drag and damping through complex fluid-structure interactions (James et al. 2006; De Langre 2008), resulting in lower-frequency, more controlled sway that distributes mechanical stresses more evenly (Vogel 1989; Spatz and Bruechert 2000; Sellier et al. 2008). In contrast, defoliated trees experience substantially reduced drag and damping (Jackson et al. 2019), leading to more vigorous motion, altered vibration characteristics, and increased stress concentrations that elevate the risk of structural failure. So, foliage effects remain an important but underexplored consideration in VA applications as they have direct implications for how wind-induced motion is encoded in visual signals.

Physics-based fluid-structure interaction models enable a controlled and independent analysis of trunk and branch dynamics. Combined with synthetic camera views, they have the potential to determine which moving components most robustly capture forces exerted by transient gusts across different wind regimes. Two main approaches used to model tree motion are a finite-element method (FEM) and a multibody approach. FEM breaks the tree into deformable elements to capture detailed bending and stress in branches and trunks (Sellier et al. 2006; Rodriguez et al. 2008; Sellier et al. 2008; Sellier and Fourcaud 2009). The multibody approach models the tree as linked rigid or flexible segments to efficiently simulate overall sway (Hadap 2006; Lv et al. 2020; Ojo and Shoele 2022; Dickinson et al. 2025). Both methods have been validated for tree dynamics and other fluid-vegetation interactions, providing a mechanistic understanding of tree sway. To date, however, no VA study has examined multi-branch tree models, so integrating modelling with VA offers the opportunity to extend current understanding of wind-tree interactions using visual signals, including extreme winds.

The present study extends VA by applying OFTV to a multibody model of two leafless trees under controlled wind forcing. We use the Elastically Articulated Body Model (EABM) from Dickinson et al. (2025) with 3D tree geometries from Calders et al. (2016). These geometry files describe the trunk and branches of a tree as a network of various-sized cylinders, which are input to the EABM to simulate wind-driven motion and generate 3D animations. The present work is the first VA study focused explicitly on defoliated trees, revealing woody structural responses and establishing a baseline for assessing the influence of foliage on wind-induced motion. Using the EABM to predict tree dynamics, we simulate motion under mean wind speeds ranging from 7 to 40 m/s (±0.25 m/s), generating modelled kinematic tree response data and associated synthetic videos. These videos are processed with the FlowOnTheGo (Weber et al. 2021a), an OFTV software, to extract pixel-wise motion, enabling spatial analysis of how the tree parts respond to increasing wind loads. By directly testing the impact of different camera angles and wind directions, our study provides practical insights that can be applied to VA to monitor movement under real-world conditions. This paper provides a step towards realising generalised VA by answering three research questions:

1. How sensitive and diagnostic is a tree's response at a range of wind speeds? i.e. up to what speeds can it potentially measure?
2. How does the camera angle relative to wind direction affect the OFTV-s_3?
3. To what extent does wind direction systematically influence the relationship between OFTV-s_3 and kinem-s_3?

2. Methods

This study employs a controlled simulation-analysis framework to quantify the sensitivity of the OFTV-s_3 to modelled kinematic response (kinem-s_3), camera angles and wind direction.

Wind-driven tree motion is first generated using the Elastically Articulated Body Model (EABM) (Dickinson et al. 2025), producing time-resolved 3D structural responses under prescribed wind conditions. The input wind forcing is defined as a time-varying signal reconstructed from discrete wind data using a Fourier-based method, providing a continuous input for the simulations. Simulations were conducted on two trees (Tree 1 and Tree 2) for each of seven input mean wind speeds that range from 7 to 40 m/s, with each run lasting 60 seconds at 50 frames-per-second (fps). The input wind forcing is extracted from an observed time series. Segments with mean wind speeds of 7-15 m/s were selected, of which 15 m/s serves as the baseline reference for a linear scaling approach used to extrapolate to higher mean wind conditions (20-40 m/s) (Supplementary Material S.1). The lower bound (7 m/s) corresponds to the minimum wind forcing available from the prescribed inflow dataset used to drive the simulations, while the upper bound (40 m/s) approaches the threshold at which structural failure would be expected in real trees.

The full details of the simulation setup, including the model formulation, input wind forcing, and numerical integration scheme, are provided in the Supplementary Material S.2.

The workflow (Figure 1, illustrated for Tree 1; identical procedures are applied to Tree 2) consists of two coupled stages: (i) a physics-based wind-structure modelled kinematic response and (ii) a vision-based motion estimation pipeline, enabling direct comparison between known modelled kinematic reference behaviour and OFTV-derived measurements.

(i) s_3 derived from simulation-based modelled kinematic reference data

From the EABM outputs (Figure 1A), modelled kinematic velocities are extracted using the perpendicular-motion decomposition, in which the component along the camera optical axis is removed and the optical-flow-visible image-plane magnitude is retained and quantified as the per-second 95th percentile magnitudes (P_{95}) (Figure 1B), providing a robust representation of extreme motion intensity (Kulkarni et al. 2026). These P_{95} values (Figure 1C, yellow dotted line) are then smoothed using a 3-second rolling mean (Figure 1C, black solid line). Maximum gusts (Figure 1C, orange squares) are subsequently identified within independent, non-overlapping 10-second analysis windows, where the maximum value of the smoothed signal defines the modelled kinematic-s_3 (kinem-s_3). Analysis windows of 10-seconds are used to match short CCTV-extractable video segments and to maintain consistency with prior VA studies that use 2-15 s observation periods (Cardona et al. 2019, 2021; Zhang et al. 2022; Kulkarni et al. 2026).

(ii) s_3 derived from OFTV, applied to video sequences from simulation

The simulated motion files created by the EABM were rendered into synthetic video sequences using ParaView version 5.12.1 (Ahrens et al. 2005). These videos are then post-processed using OFTV software, FlowOnTheGo (Weber et al. 2021b) (Section 2.1). Each 60-second video from the simulation was partitioned into six non-overlapping 10-second segments for independent gust estimation. As shown in Figure 1 (D-F), frame-to-frame displacements are used to reconstruct motion fields, from which raw OFTV magnitudes are derived (Figure 1D). These are then directionally filtered (details in Section 2.1) to isolate wind-aligned motion and exclude some non-wind-aligned artefacts created by the trunk, and the resultant P_{95} is used to represent dominant movement (Figure 1E). Time-series analysis of the P_{95} signal (Figure 1F, blue dotted line) and subsequent 3-sec rolling mean (Figure 1F, black solid line), enables the extraction of OFTV-s_3 (Figure 1F, red markers) within independent, non-overlapping 10-second analysis windows. This forms the OFTV-s_3 metric used throughout this study. Stages (i) and (ii) use identically defined, non-overlapping 10-second analysis windows, ensuring direct temporal alignment between kinem-s_3 and OFTV-s_3.

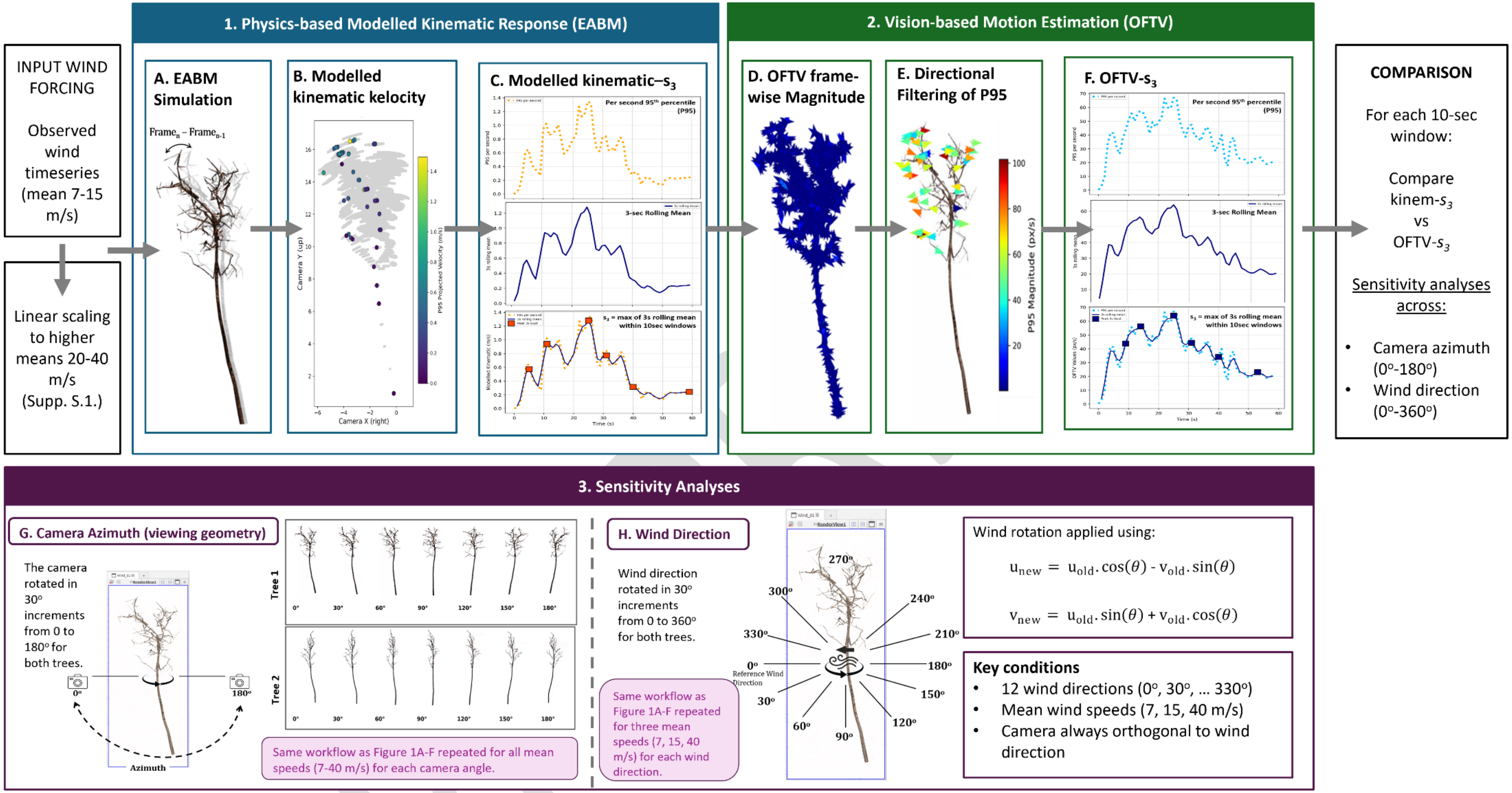

Figure 1: Overview of the simulation-analysis workflow used to derive peak 3-second gusts (s_3) (Tree 1 shown for illustration; identical procedure applied to Tree 2). (A) Representative pair of frames from the completed EABM simulation, forming the starting point of the analysis workflow. Kinematic pathway:(B) Spatial distribution of modelled kinematic velocities projected into the camera's view. (C) Time series of magnitude of the velocity vectors showing the per-second 95th percentile (P_{95}) signal (orange dotted line), corresponding 3-second rolling mean (black solid line), and extracted s_3 values (orange markers), defined as the maximum of the smoothed signal within independent 10-second windows. OFTV pathway: (D) Frame-to-frame optical flow magnitude field derived from synthetic video sequences. (E) Directional filtering applied to retain motion within ±20° of the dominant wind-flow direction in the vertical plane. (F) Time series of P_{95} OFTV magnitude (blue dotted line) and corresponding 3-second rolling mean (black solid line), from which s_3 is extracted (red markers) within independent 10-second windows. Sensitivity analysis: (G) camera azimuth varied from 0° to 180° to assess the influence of viewing geometry on OFTV-s_3. (H) wind forcing direction rotated from 0° to 360° to evaluate the directional dependence of the OFTV-s_3.

Lastly, to systematically evaluate sensitivity, two independent sources of variability are introduced. First, camera horizontal viewpoints were varied by adjusting the azimuth angle of the camera in 30° increments, covering views from 0° to 180° (Figure 1G; Top and Bottom for Tree 1 and Tree 2, respectively), to assess the influence of viewing geometry. Here, 0° is parallel to the baseline, initial incoming wind vector. Only 0-180° camera angles were analysed because opposite views yield similar structural projections. Second, the direction of the applied wind forcing is rotated from 0° to 360° (Figure 1H) to assess whether tree asymmetry introduces directional dependence in OFTV-s_3. To evaluate the effect of wind orientation, 11 rotated wind directions were generated for mean wind speeds of 7, 15, and 40 m/s. These were incrementally rotated by 30° intervals (30°, 60°, …, 300, 330°) around the vertical axis. For each wind direction, the camera was rotated such that its viewing direction remained orthogonal to the wind vector (i.e., offset by 90° relative to the wind direction). This ensured a constant wind-camera geometry across all simulations. For both, Figure 1G and Figure 1H, the same workflow described in Figure 1A-F is repeated, ensuring consistency in s_3-extraction across all camera angles and wind directions.

2.1. Data Processing

The videos were processed using FlowOnTheGo (Weber et al. 2021a) with all the software details in Supplementary Material S.3.

The optical flow equation relates the change in pixel intensity over time to velocities in both the x- and y-directions. The horizontal and vertical velocity components were calculated by taking the difference between the x- and y-particle positions of data points in consecutive frames and dividing by the corresponding time duration. The velocity magnitude was calculated using the Euclidean norm.

To reduce contamination from non-wind-aligned motion components in the optical flow signal, particularly large apparent vertical motions at the trunk's edge as it oscillates horizontally, a directional filter was applied to isolate lateral motion associated with wind-driven deformation (Supplementary Material S.4). A ±20° directional filter was applied to retain motion aligned with the dominant wind-flow direction while suppressing vertically oriented trunk motion. This retained ~21-28% of velocity vectors and ~16-24% of total motion magnitude, while preserving strong wind-motion relationships.

2.2. Regression and Performance Evaluation

Linear relationships between kinem-s_3 and OFTV-s_3 were quantified using ordinary least squares (OLS) regression:

$$\hat{y} = \beta x + \alpha \quad (1)$$

Where x represents kinem-s_3 values, $\hat{y}$ represents predicted OFTV-s_3, β is the regression slope describing the scaling relationship between OFTV-s_3 and kinem-s_3, and α is the intercept. Regression uncertainty was estimated using non-parametric bootstrap resampling of paired kinem-s_3 and OFTV-s_3 observations (2000 iterations) with the regression refitted for each resample. The 95% confidence intervals for β were derived from the 2.5th and 97.5th percentiles of the bootstrap slope distribution. Unlike a previous study (Kulkarni et al., 2026) where TLS accounted for uncertainty in both OFTV and anemometer data, OLS was used here because there is no observational uncertainty in the kinematic reference data. To enable comparison with prior studies, the standard metrics computed are R^2, Root Mean Square Error (RMSE) and Mean Absolute Percentage Error (MAPE). MAPE was calculated as:

$$\mathrm{MAPE} = \frac{100\%}{\mathrm{n}} \sum_{\mathrm{i}=1}^{\mathrm{n}} \left| \frac{\mathrm{y_i} - \hat{\mathrm{y}}_\mathrm{i}}{\mathrm{y_i}} \right| \tag{2}$$

where y_i represents kinem-*s₃*, $\hat{y}_i$ are regression predictions, *n* is the number of observations, and $\bar{y}$ is the mean of observed values.

2.3. Camera Angles and Wind Direction Analysis

To evaluate whether camera angle influenced OFTV performance (Results Section 3.3), two limiting projection models, termed the pole model and null model, were considered. At one extreme, a pole model (Results 3.3., Figure 5B) is analogous to a single degree-of-freedom representation, in which the tree trunk and canopy combined are approximated as a single oscillating mass with one dominant natural frequency and a fixed axis of sway (Miller 2005; James et al. 2014). This is the simplest form of the cantilever-beam idealisation used throughout tree-sway modelling (James et al. 2006; Sellier and Fourcaud 2009; Pivato et al. 2014), producing the angle-dependent projection signature of single-mode, directionally coherent motion. In this simplified case, the tree is assumed to oscillate predominantly parallel to the mean vector of the forcing wind, such that motion is minimised when viewed along the direction of motion (0° and 180°) and maximised when viewed perpendicular to it (90° and 270°). This idealised angular response can be represented as:

$$y_{pole}(\theta) \approx A + B|\sin(\theta)| \tag{3}$$

where θ is the camera viewing angle, A is the mean response, and B is the amplitude of angular modulation.

At the other extreme, a null (isotropic) model (Results 3.3., Figure 5B) is derived from the multi-degree-of-freedom idealisation, in which branches behave as additional, weakly coupled oscillating masses attached to the trunk rather than moving in unison with it (James et al. 2006; De Langre 2008; Rodriguez et al. 2008, 2012). Because motion is distributed across multiple modes rather than one dominant, directionally aligned mode, no stable camera-angle-dependent projection signature is expected: $y_{null}(\theta) = A$.

These models represent conceptual end-members rather than complete descriptions of tree dynamics. As camera angles were sampled only from 0°-180°, only the peak at 90° is directly observable; the second peak at 270° is the symmetric continuation implied by periodicity. Therefore, a phase-shifted second-harmonic cosine model was fitted:

$$y(\theta) = A + B\cos(2\theta + \phi) \tag{4}$$

where θ is the camera angle, A is the mean response, B is the angular modulation amplitude, and ϕ is the phase shift. The phase term allows peak and minimum responses to vary from the idealised pole-model orientations. An *F*-test compared the cosine model with the constant null model, with significance assessed at $p < 0.05$.

To evaluate wind direction effects on OFTV-s_3, Equation (3) was fitted through the origin for each wind direction and wind speed to obtain the directional regression slope (β). Directional variation in OFTV response was further assessed by fitting the cosine model (Equation 7) to directionally aggregated observations. Here, θ represents wind direction, A is the mean response, B is the amplitude of directional modulation, and ϕ represents the preferred wind direction associated with maximum response. Unlike camera angle, which repeats over 180°, wind direction spans 360°, so a single cosine term was used to capture directional asymmetry in tree response.

$$y(\theta) = A + B\cos(\theta - \phi) \tag{5}$$

3. Results

The Results section first examines the fundamental wind-structure relationship in the two simulated trees (Section 3.1), comparing input wind forcing with kinem-s_3 responses to establish the underlying dynamical behaviour of tree motion. Section 3.2 then evaluates the performance of OFTV-s_3 as a proxy for kinem-s_3 motion. Building on this, Section 3.3 investigates the influence of viewing geometry by assessing the sensitivity of OFTV-s_3 to camera angle (0°-180°). Finally, Section 3.4 extends the analysis to environmental anisotropy by examining the effect of wind direction (0°-330°) on OFTV-s_3 and its relationship with kinem-s_3.

3.1. Wind-driven acceleration response of tree motion

Figures 2A-B show that kinem-s_3 increases approximately linearly with input wind speed for both Tree 1 (R^2 = 0.87) and Tree 2 (R^2 = 0.90), indicating that observed velocities are a useful measure of the integrated structural response of the tree system to wind forcing. Modelled kinematic acceleration, however, for both Tree 1 (R^2 = 0.98; RMSE = 1.19) and Tree 2 (R^2 = 0.96; RMSE = 2.09) exhibits nonlinear scaling. Figures 2C-D present raw acceleration versus wind speed with quadratic fits, showing that acceleration increases faster than linearly with wind speed and is consistent across specimens. Figures 2E-F show power-law fits to quantify the nonlinear relationship, with the log-log gradients close to the theoretical value of 2 expected for quadratic scaling (Munson et al. 1998; Simiu and Yeo 2019) for both trees (Tree 1 = 1.8; Tree 2 = 1.9). This provides strong evidence that tree acceleration scales approximately with the square of wind speed, where wind-induced forces increase with wind velocity squared due to dynamic pressure effects (Vogel 1994; De Langre 2008). As acceleration directly reflects changes in velocity over time, it provides a measure of the instantaneous dynamic response of the tree system to wind forcing (James et al. 2006; Gardiner et al. 2016a).

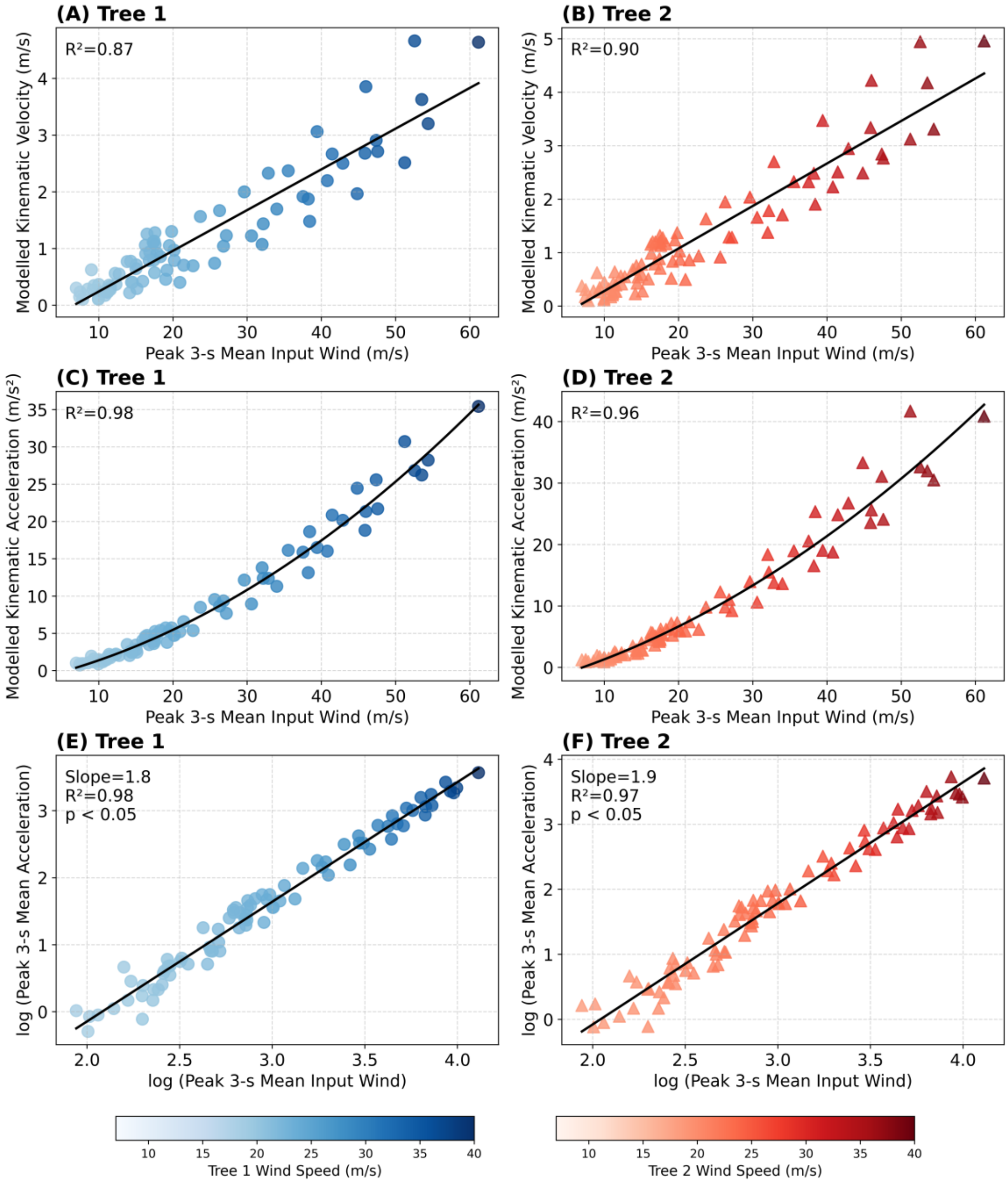

Figure 2: Relationship between input wind speed (x-axis) and measured modelled kinematic tree response (y-axis) for Tree 1 (A, C, E) and Tree 2 (B, D, F) under controlled conditions. Panels A-B show velocity, panels C-D show raw acceleration with quadratic fits, and panels E-F show the log of acceleration (power-law scaling). Trend lines indicate linear fits for velocity and quadratic/power-law fits for acceleration.

Overall, these results mechanistically link modelled velocity vectors to wind forcing via tree acceleration using well-established physics (see Discussion section 4.1). This insight is necessary as OFTV captures motion through frame-to-frame displacement and is therefore primarily configured to detect velocity rather than acceleration. Although acceleration can be derived from velocity time series, this may introduce additional uncertainty due to temporal differentiation and potential changes in tracked features between consecutive frames. Section 3.2 takes the next logical step, evaluating OFTV as a proxy for observing tree motion velocity vectors.

3.2. Evaluation of OFTV as a Proxy for Wind-Driven Tree Motion

Figure 3 evaluates the utility of OFTV velocities (px/s) as a proxy to capture modelled kinematic tree motion, with kinem-s_3 (m/s) used as the reference physical response variable. Tree 1 (Figure 3A) has an R^2= 0.96, and Tree 2 (Figure 3B) has an R^2= 0.93. Both relationships are statistically significant ($p < 0.05$). These results indicate that OFTV captures a substantial proportion (>90%) of variability in kinem-s_3.

Table 1: Performance metrics (R^2, RMSE, and MAPE) for OFTV as a proxy for modelled kinematic tree velocity.

Tree	**Slope**	R^2	**RMSE (px/s)**	**MAPE (%)**
(A) Tree 1	42.96	0.96, $p < 0.05$	9.21	17.16
(B) Tree 2	41.03	0.93, $p < 0.05$	12.85	10.79

Table 1 summarises performance metrics (R^2, RMSE, and MAPE) for OFTV as a proxy for kinem-s_3. Tree 1 shows lower error and higher explanatory power than Tree 2, suggesting differences in structural or imaging sensitivity between specimens. The difference in performance likely reflects variations in branching architecture, motion coherence, self-occlusion, or image texture, all of which are known to influence optical flow estimation in deformable scenes (Sun et al. 2014; Sevilla-Lara et al. 2014; Zille et al. 2014).

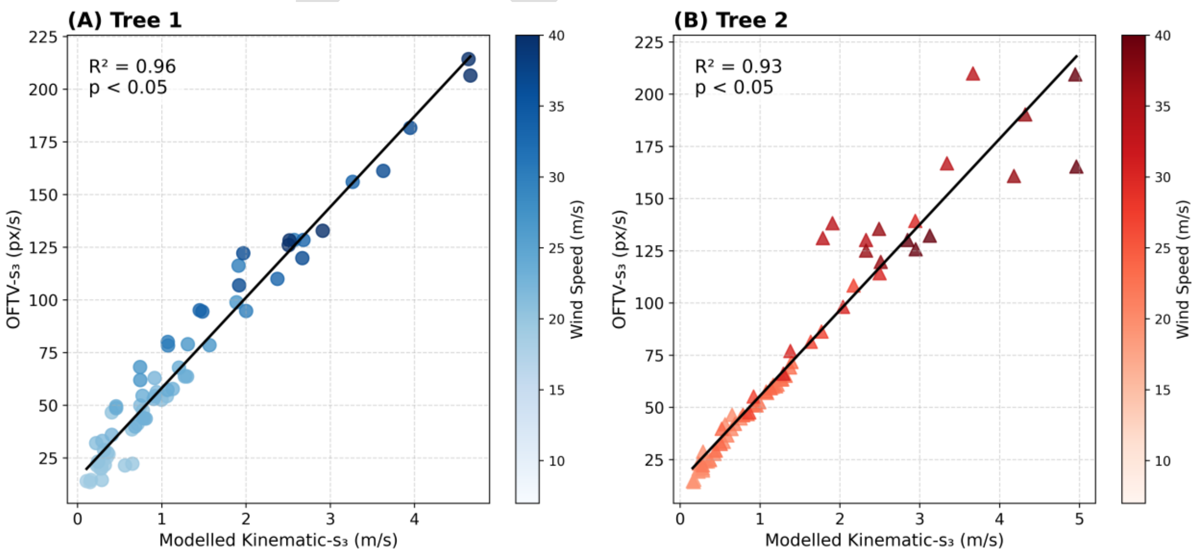

Figure 3: Scatter plots of kinem-s_3 (m/s) and OFTV-s_3 (px/s) for (A) Tree 1 and (B) Tree 2 under multiple wind speed conditions (7–40 m/s). Each point represents the maximum value extracted from 10-second independent windows of 3-second rolling-mean time series. Points are coloured by wind speed, with darker shades indicating higher wind speeds. The black line shows the linear regression fit across all wind conditions.

3.3. Camera angle effect on OFTV-s_3

Figure 4 presents the R^2 between OFTV-s_3 and kinem-s_3 across camera viewing angles from 0° to 180° for Trees 1 and 2. For Tree 1 (Figure 4A), R^2 ranged from 0.94 to 0.99, with the highest value observed at 90°, while for Tree 2 (Figure 4B), R^2 ranged from 0.93 to 0.99, with the highest value observed at 120°. For both trees, a cosine fit (black dotted line; Equation 5) had a small amplitude (B = −0.018 and −0.011, respectively) and did not significantly improve upon the null model (grey dashed line) (Tree 1: F = 2.80, p > 0.05; Tree 2: F = 0.49, p > 0.05), indicating no clear evidence that R^2 varies with camera angle. So, overall, R^2 remains high and stable across all viewing directions, indicating that VA performance is not strongly affected by camera angle.

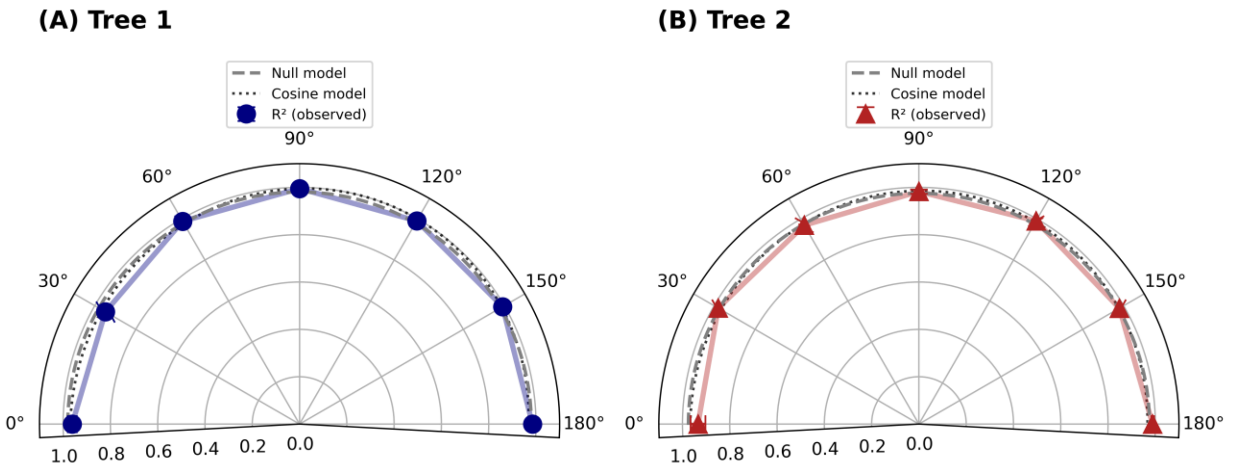

Figure 4: Polar plots show the variation in observed R^2 between OFTV-s_3 vs kinem-s_3 regression across camera viewing angles (0-180°) for (a) Tree 1 and (b) Tree 2 for all tested wind speeds. Points represent OFTV-s_3 vs kinem-s_3 regression R^2 with error bars as the 95% confidence intervals. The black dotted line represents the fitted cosine model (Equation 5), fitted to the observed R^2 values as a function of camera viewing angle, while the grey dashed line represents the fitted null (constant) model.

Figure 5A shows how the regression slope (β) between OFTV-s_3 and kinem-s_3 changes with camera angle (0°-180°), with the conceptual end-member models shown in Figure 5B. For Tree 1 (Figure 5A), the mean β was 44.92, with a cosine model amplitude of B = 4.85 (Equation 5). Although the cosine model described part of the angular variation (R^2 = 0.676), it did not significantly improve on the null model (F = 4.18, p > 0.05). Tree 2 showed a similar response (mean β = 45.55, B = 5.77), with no significant angular dependence (F = 1.88, p > 0.05) despite a moderate cosine fit (R^2 = 0.484). Regression errors remained low (mean RMSE = 7.35 and 8.89, MAPE = 9.56% and 8.16% for Trees 1 and 2, respectively). Overall, both trees were closer to the null model than the strong pole model (Figure 5B).

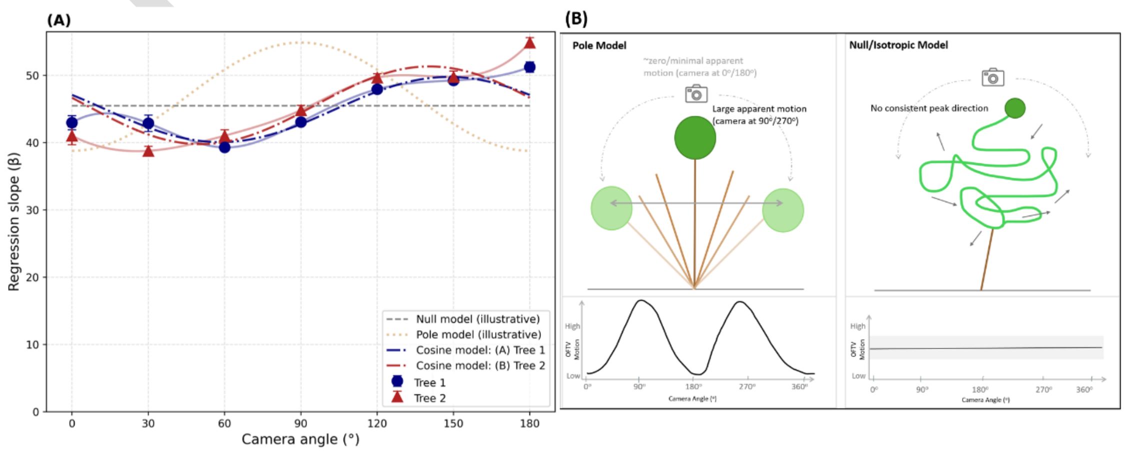

Figure 5: (A) Relationship between regression slope (β) (pxs^{-1}/ms^{-1}) and camera angle for Tree 1 and Tree 2. Data points show the fitted slope values at each camera angle (0°-180°). The dashed coloured (blue for Tree 1 and red for Tree 2) lines represent the fitted cosine model (Equation 6), the orange and grey dotted/dashed lines indicate the rigid pole model (Equation 5) and the angle-independent null model, respectively, which are illustrative and are not fitted to experimental data. Error bars show the 95% confidence interval of the regression R^2. (B) A qualitative end-member sketch of the rigid-pole model and a null model (Methods Section 2.3). The pole model (left) produces a clean, axis-aligned response with maximal apparent motion at 90°/270° and near-zero at 0°/180°, whereas the null model (right) exhibits non-axis-aligned, multi-directional excursions with no preferred orientation.

Figure 6 shows the camera-angle sensitivity of OFTV-*s₃* with increasing wind speed, represented by the mean regression slope (β) and its standard deviation (σ) across camera angles. For Tree 1, β remained stable across 7-40 m/s, with no significant trend ($p > 0.05$). For Tree 2, β decreased over the full range ($p = 0.033$), but not for wind speeds ≥15 m/s ($p > 0.05$). This indicates that the apparent decrease may reflect differences between the independent 7-15 m/s wind inputs and those used for extrapolated higher-wind simulations. Angular variability showed no consistent wind speed dependence for either tree. Thus, increasing wind speed did not produce a systematic increase in directional, geometry-dependent tree motion, as might be expected if the response progressively shifted from isotropic (null) motion of smaller branches towards coherent, pole-like swaying of the whole tree. Significant angular effects at 8 and 12 m/s were isolated and did not represent a persistent transition.

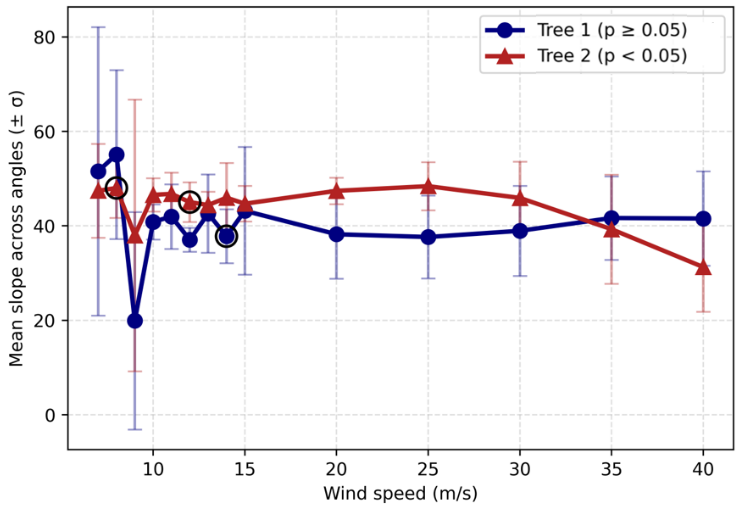

Figure 6: Mean regression slope (β) (pxs^{-1}/ms^{-1}) across camera orientations as a function of wind speed for Tree 1 and Tree 2. Markers show the mean slope across measured camera angles, and error bars show the standard deviation (σ) among angles. Black outlines indicate wind speeds with a significant angular effect based on the cosine-versus-null model comparison ($p < 0.05$).

3.4. Anisotropic tree response to wind direction and implications for OFTV-s_3

Table 2: Mean regression slope (β), standard deviation (σ), and coefficient of variation (CV) for the OFTV-s_3 vs kinem-s_3 relationship across wind speeds.

Tree	Wind speed (m/s)	Mean β	σ	CV (%)
Tree 1	7	96.98	16.77	17.3
	15	64.49	20.40	31.6
	40	48.03	6.10	12.7
Tree 2	7	127.41	23.84	18.7
	15	68.74	19.59	28.5
	40	48.29	5.79	12.0

Figure 7 shows that the regression slope (β) (px/s) between OFTV-s_3 and kinem-s_3 varied with wind speed but showed no consistent dependence on wind direction for either tree. β decreased by ~50-62% between 7 and 40 m/s (Table 2). Although this may indicate increasing nonlinearity, Figure 3 shows that the OFTV-s_3-kinem-s_3 relationship remains approximately linear, with no clear saturation. The lower β likely reflects changes in tree biomechanics and/or optical representation of motion at higher wind speeds. Variability in β across wind directions increased at 15 m/s before decreasing at 40 m/s, with CV values reducing to 12.7% for Tree 1 and 12.0% for Tree 2 at 40 m/s. Bootstrap confidence intervals similarly narrowed at higher wind speeds. Together, the OFTV-kinematic scaling became more consistent across wind directions as wind speed increased, despite the reduction in β.

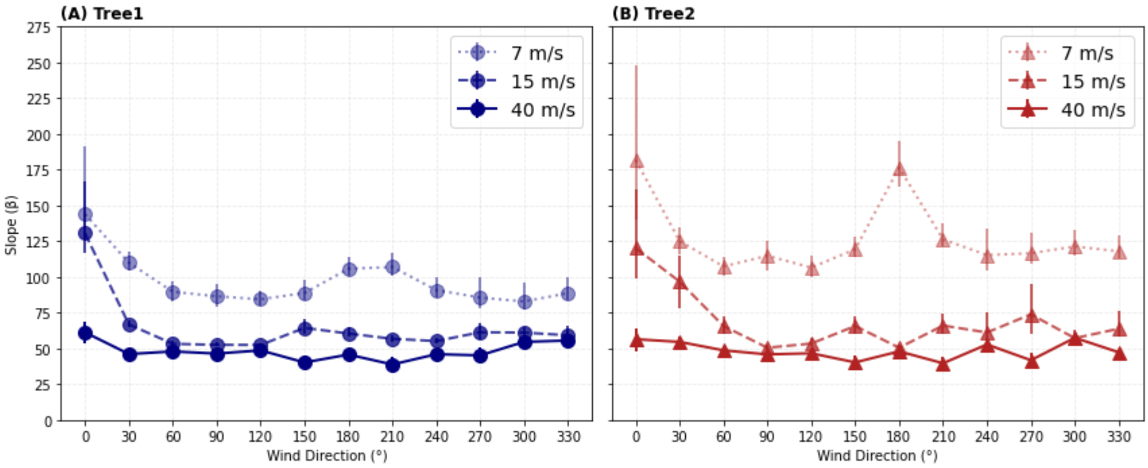

Figure 7: Slope coefficients (β) obtained from origin-constrained linear regressions between kinematic wind speed and OFTV-derived response metrics for each wind direction (0°-330°) and wind speed (7, 15, and 40 m/s) for Tree 1 and Tree 2. Points show mean slope estimates per direction, while error bars represent 95% confidence intervals derived from bootstrap resampling. Blue and red colours denote Tree 1 and Tree 2, respectively.

Figure 8 shows the results of fitting a cosine model to test whether extracted OFTV-s_3 peaks vary systematically with wind direction. A significant anisotropic response was observed at 7 and 15 m/s for both trees (Table 3), but was not significant at 40 m/s ($p > 0.05$). The reduced directional dependence at high wind speed indicates that OFTV-s_3 becomes more robust to wind orientation under stronger wind conditions. This trend agrees with the reduced β variability shown in Figure 7 and Table 2, where CV decreased with wind speed.

Table 3: Cosine-vs-null model fit statistics for OFTV-s_3 directional dependence at each wind speed for Tree 1 and Tree 2. Values show the fitted cosine amplitude (B), preferred direction (φ), R^2, F-statistic, and p-value for comparison with the direction-independent null model. Significant directional dependence is indicated by $p < 0.05$.

Tree	Wind speed (m/s)	B	ϕ (°)	R^2	F	*p*
Tree 1	7	0.175 ± 0.025	17.2 ± 4.2	0.41	23.80	<0.05
	15	0.147 ± 0.043	7.4 ± 8.4	0.14	5.78	<0.05
	40	−0.038 ± 0.032	14.7 ± 24.6	0.02	0.68	0.51
Tree 2	7	0.210 ± 0.040	1.6 ± 5.5	0.28	13.74	<0.05
	15	0.207 ± 0.051	27.0 ± 7.1	0.19	8.21	<0.05
	40	0.063 ± 0.036	46.5 ± 16.4	0.04	1.53	0.22

Together, these results indicate that directional effects are strongest at lower wind speeds and become weak as wind-driven motion dominates at higher speeds.

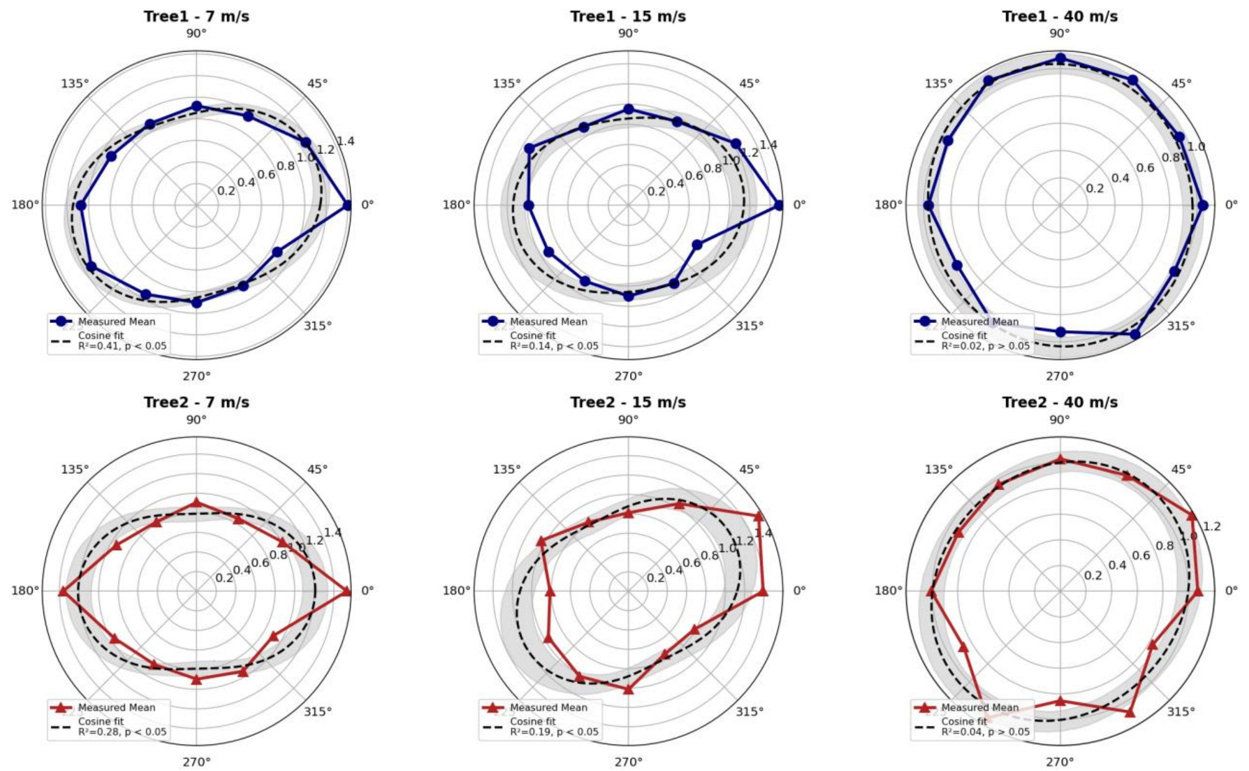

Figure 8: Polar plots of the normalised OFTV-s_3 response as a function of wind direction for Tree 1 and Tree 2 at wind speeds of 7, 15, and 40 m/s. Markers show the mean normalised OFTV-s_3 for each wind direction, and the dashed line shows the fitted cosine model (Equation 7). Grey shading indicates the 95% bootstrap confidence interval, R^2 indicates goodness of fit, and F-test significance compares the cosine model with the null model. Normalisation was performed independently for each tree and wind speed by dividing OFTV-s_3 by its mean across all wind directions.

4. Discussion

This study evaluates Optical Flow Tracking Velocity (OFTV) in visual anemometry using defoliated tree simulations to allow extreme wind regimes (i.e. up to 40 m/s) to be considered, which are rarely captured in field observations where safety, instrumentation limits, and data availability constrain measurements (James and Kane 2008; Hao et al. 2020; Zanotto et al. 2024).

4.1. Scaling Behaviour of Wind-Driven Tree Motion

The first line of investigation is into how sensitive and diagnostic a tree's response is at a range of wind speeds. Figure 2C-F is a verification that the EABM simulated wind-driven tree motion behaves as a forced multibody dynamical system in which applied forces govern acceleration and exhibit a strong nonlinear dependence on wind speed (Featherstone 1987; Dowell and Hall 2001). This is a fundamental feature of flexible body formulations used in biological and robotic systems (Calders et al. 2016; Dickinson et al. 2025), aligning with classical fluid-structure interaction theory, where drag scales with the square of wind velocity (De Langre 2008; Gosselin 2019). Importantly for visual anemometry (VA), however, observed velocity also scales with wind speed, approximately linearly. The slightly lower correlation (R^2 ~ 0.87, p < 0.05) is consistent with it being a more indirect representation of aerodynamic forcing than acceleration

(Figure 2A-B). In a second necessary step, the strong agreement (Figure 3, R^2 ~ 0.9, p < 0.05) between OFTV-s_3 and kinem-s_3 indicates that the frame-to-frame velocities calculated by OFTV capture a substantial proportion (i.e. >90%) of structural motion variability under controlled conditions, supporting its use as a proxy for wind speed.

Previous VA studies have assumed a linkage between vegetation motion and wind forcing, for example, quantifying the relationship using neural networks such as CNN-LSTM based on tree sway (Cardona et al. 2019; Zhang et al. 2022), physics-based bending and sway models (Cardona et al. 2021; Cardona and Dabiri 2022), and spectral decomposition methods applied to dynamic motion fields (Runia et al. 2020). Kulkarni et al. (2026) reported that the performance of OFTV-derived gusts depends on species and canopy structures in a real-world domestic setting. The MAPE observed in the present study (~10-17%; Table 1) is lower than their values reported (31.9-47.9%) due to the use of an idealised modelled structural response rather than in situ wind measurements. The previous studies primarily evaluated foliated canopies under moderate wind speeds (<15 m/s). So, by examining wind speeds of up to 40 m/s and by mechanistically justifying the motion-wind-velocity relationship, the present work provides evidence that VA should be robust under extreme winds and substantially stronger structural loading.

With OFTV established as a valid observational analogue of kinematic motion, it is possible to examine the effects of viewing geometry and wind direction on wind speed estimation.

4.2. Influence of viewing geometry on OFTV performance

By conducting an explicit evaluation of the influence of multiple viewing angles, the correspondence between OFTV-s_3 vs. kinem-s_3 remained consistently strong (R^2 ≈ 0.9; Figure 4) for both trees, while the amplitudes of the fitted cosine functions were close to zero, and neither showed statistically significant angular modulation (Figure 4). This result is important because it indicates that the statistical relationship between image-derived motion and wind-related tree kinematics is not strongly dependent on the viewing geometry for the two trees tested here. In practical terms, this suggests that VA may remain feasible under opportunistic camera placement, where the viewing geometry is not known or controllable in advance. Multiple viewing angles have been implicitly included in VA studies (Zhang et al. 2022), or studying trees from a top-view (Dabiri et al. 2023), but without considering the impact of this.

Figure 5A further showed no statistically significant angular dependence of the OFTV-s_3-kinem-s_3 scaling slope (β) for either tree; although the cosine model captured some descriptive variation (R^2 = 0.6 and 0.4), the response was not consistent with the strong projection effect expected for an idealised rigid pole and instead more closely resembled the angle-independent null model in Figure 5B. This agrees with tree-biomechanics research showing that, while classical beam models predict a dominant bending response aligned with the mean wind direction (James et al. 2006; Sellier and Fourcaud 2009; Pivato et al. 2014), branched trees exhibit motion across multiple structural components and vibration modes (Rodriguez et al. 2008, 2012). Such isotropic responses arise from turbulent forcing across multiple spatial and temporal scales, from branch motion to whole-crown reconfiguration (Finnigan 2000; Gardiner et al. 2016b). Previous VA approaches have represented tree motion using a cantilever beam (Cardona et al. 2021) or damped single-degree-of-freedom oscillator models (Cardona and Dabiri 2022). The former estimated wind speed from mean deflection and performed well for cylinders and some trees but degraded at higher winds as large deformations violated linear beam assumptions. The latter used sway amplitude, improving applicability to larger trees but still assuming modal dominance. Zhou et al. (2023) used geometric models to estimate wind from a single lightweight stick. As a rigid element, its wind estimates were sensitive to the camera viewpoint. Data-driven methods (Zhang et al. 2022) have inferred wind conditions from vegetation motion without explicitly testing camera orientation. In contrast, our results show that, deviating from the pole model, trees can produce an angle-robust wind signal, with low and stable prediction errors across viewing angles (Figure 5A; mean RMSE = ~7-8 px/s; MAPE = ~8-9.5%). This supports the wider potential of VA based on existing cameras or crowdsourced video, where camera placement is rarely optimised for tree structure.

Figure 6 further tests whether the balance between these two conceptual end-member models (Figure 5B) changes with wind speed. Although increasing wind speed could potentially promote more coherent, whole-tree motion, neither tree showed a consistent increase in angular variability across 7-40 m/s. The apparent decrease in β for Tree 2 was not significant when considering only wind speeds ≥15 m/s. Overall, the results provide no evidence for a systematic shift towards a more pole-like response with increasing wind speed. The pole-like and null responses should therefore be regarded as conceptual end-members of a continuum influenced by tree architecture, foliage, and wind characteristics (Baker 1997; Rodriguez et al. 2012). For the trees tested here, the absence of a persistent directional transition supports the practical use of OFTV without requiring precise camera alignment to a structural axis.

4.3. Directional Anisotropy in OFTV-s_3

VA studies to date (e.g., Cardona et al. 2019; Runia et al. 2020; Zhang et al. 2022), have not explicitly tested the effects of directionality; however, studies (Cardona et al. 2021; Cardona and Dabiri 2022; Kulkarni et al. 2026) report consistent incident wind direction during data collection. Physics-based VA studies (e.g., Cardona et al. 2021; Dabiri et al. 2023) have primarily examined mean deformation or RMS motion rather than directional anisotropy in high-frequency motion metrics, despite a theoretical framework (Dickinson et al. 2025) that predicted direction-dependent vegetation responses arising from centre-of-mass asymmetry.

By varying wind direction while maintaining the camera perpendicular to the flow, this study isolates directional effects on OFTV-s_3. The results show that directional sensitivity is dependent on wind speed: significant anisotropic responses were observed at 7 and 15 m/s, but were not significant at 40 m/s (Figure 8). This reduction in directional dependence at high wind speeds is consistent with the reduced variability in β across wind directions (Figure 7; Table 2), suggesting that stronger forcing produces a more consistent

OFTV response across orientations. At lower wind speeds, directional effects may arise because wind-induced motion is distributed across individual branches and influenced by tree architecture, increasing the contribution of local motion to the extracted visual signal (Spatz and Bruechert 2000; Sellier and Fourcaud 2009; Pivato et al. 2014). As wind forcing increases, stronger aerodynamic loading and structural reconfiguration promote more coherent whole-tree motion (Raupach 1992; Finnigan 2000; De Langre 2008), reducing the relative influence of orientation-dependent structural effects. Similarly, turbulent canopy flows become increasingly dominated by larger-scale coherent motions as mean wind strength increases (Raupach 1992; Finnigan 2000).

Practically, these results show that OFTV-s_3 remains reliable under strong winds, supporting its use for estimating extreme winds from tree videos even where wind direction is unknown. Although lower wind speeds may require consideration of directional effects, the robust high-wind performance highlights its wide potential for real-world monitoring.

4.4. Limitations and Implications for Future Applications

Firstly, the highest simulated wind speeds exceed the range in which real trees behave as purely elastic structures. Under strong winds, trees typically enter non-linear regimes involving branch breakage, progressive reconfiguration, or stem failure (Vogel 1994; Niklas and Spatz 2000). For this reason, these simulations should be interpreted as controlled stress tests of the OFTV framework rather than literal representations of tree biomechanics. Extending the dynamic range nevertheless provides a useful way to evaluate the stability and sensitivity of OFTV across conditions relevant to extreme wind events.

Secondly, the modelling framework simplifies complex vegetation-flow interactions, with OFTV primarily capturing visible canopy motion rather than detailed trunk or branch deformation. Fine-scale canopy elements can contribute strongly to optical-flow signals due to their rapid aerodynamic response (Rudnicki et al. 2001; De Langre 2008). In addition, certain physical processes such as 3D flow sheltering effects and full canopy reconfiguration are not explicitly represented, which may introduce additional variability in more complex environments.

Finally, real-world field deployments may be influenced by wind-direction variability and observation geometry. In the simulations, gravitational asymmetry is absent, so directional differences arise mainly from structural geometry. In natural environments, persistent directional wind patterns driven by topography or canopy heterogeneity (Finnigan 2000; Belcher et al. 2012) may influence OFTV scaling and uncertainty. This highlights the importance of camera placement relative to prevailing winds in future operational or multi-site applications.

5. Conclusions and Future Work

The present study evaluated Optical Flow Tracking Velocimetry (OFTV) as a physics-consistent, video-based proxy for peak 3-second gust wind speed (s_3) in defoliated tree models under controlled wind forcing up to 40 m/s, providing a mechanistic extension of previous visual anemometry (VA) approaches. It is the first visual anemometry study to examine defoliated trees, to use simulations of trees to extend mechanistic understanding to extreme wind speeds, to examine the impact of camera angle and to explicitly consider incident wind direction. The main findings are as follows:

1. Across simulations, OFTV-s_3 showed strong agreement with the underlying kinematic response ($R^2 \approx 0.9$), which scales with the input wind speed, demonstrating that optical flow captures coherent structural motion even under nonlinear wind–structure interactions.

2. Camera viewing geometry does not significantly modulate OFTV amplitude or degrade predictive performance ($R^2 \approx 0.9$), with no statistically significant angular dependence detected in either correlation strength or scaling slope (β) across 0°-180° viewing angles. Although β showed modest directional variation, wind speed did not produce a systematic increase in angle sensitivity, indicating robustness to camera orientation under the tested conditions.

3. OFTV-s_3 showed reduced sensitivity to horizontal wind direction at higher wind speeds, with directional effects becoming weak under strong wind forcing.

Future work should extend this framework to foliated and heterogeneous canopies to assess how aerodynamic complexity affects signal coherence under real-world turbulent conditions. Field studies on defoliated trees across seasonal cycles would enable testing of temporal evolution in OFTV performance, particularly how transitions between leaf-on and leaf-off states influence signal stability and scaling. Further work could also explore the technical video effects (e.g., frame rate, resolution, etc.) and whether wind direction can be reliably extracted from video-based measurements of tree motion, which remains an important question raised by this study. Finally, comparisons with data-driven methods such as machine learning-based visual anemometry would help position OFTV within the broader landscape of wind inference techniques.

Overall, this study demonstrates that OFTV-s_3 provides a robust and physically interpretable measure of vegetation motion. Importantly, and in contradiction to initial expectations, the results highlight that wind magnitude is the dominant control on observed motion, with directional effects and viewing geometry having a limited influence on OFTV-s_3 performance.

References

Ahrens, J., B. Geveci, and C. Law, 2005: *ParaView: An End-User Tool for Large Data Visualization, Visualization Handbook*. Elsevier.

Baker, C. J., 1997: Measurements of the natural frequencies of trees. *J Exp Bot*, **48**, 1125–1132, https://doi.org/10.1093/jxb/48.5.1125.

Belcher, S. E., I. N. Harman, and J. J. Finnigan, 2012: The Wind in the Willows: Flows in Forest Canopies in Complex Terrain. *Annual Review of Fluid Mechanics*, **44**, 479–504, https://doi.org/10.1146/annurev-fluid-120710-101036.

Calders, K., A. Burt, N. Origo, M. Disney, J. Nightingale, P. Raumonen, and P. Lewis, 2016: Large-area virtual forests from terrestrial laser scanning data. *2016 IEEE International Geoscience and Remote Sensing Symposium (IGARSS)*, 1765–1767, https://doi.org/10.1109/IGARSS.2016.7729452.

Cardona, J., M. Howland, and J. Dabiri, 2019: Seeing the Wind: Visual Wind Speed Prediction with a Coupled Convolutional and Recurrent Neural Network.

Cardona, J. L., and J. O. Dabiri, 2022: Wind speed inference from environmental flow–structure interactions. Part 2. Leveraging unsteady kinematics. *Flow*, **2**, E1, https://doi.org/10.1017/flo.2021.15.

——, K. L. Bouman, and J. O. Dabiri, 2021: Wind speed inference from environmental flow–structure interactions. *Flow*, **1**, E4, https://doi.org/10.1017/flo.2021.3.

Cusack, S., 2023: A long record of European windstorm losses and its comparison to standard climate indices. *Natural Hazards and Earth System Sciences*, **23**, 2841–2856, https://doi.org/10.5194/nhess-23-2841-2023.

Dabiri, J. O., M. F. Howland, M. K. Fu, and R. H. Goldshmid, 2023: Visual anemometry for physics-informed inference of wind. *Nat Rev Phys*, **5**, 597–611, https://doi.org/10.1038/s42254-023-00626-8.

De Langre, E., 2008: Effects of Wind on Plants. *Annu. Rev. Fluid Mech.*, **40**, 141–168, https://doi.org/10.1146/annurev.fluid.40.111406.102135.

Dickinson, R. E., T. I. Marjoribanks, C. J. Keylock, and A. Palmeri, 2025: Modelling vegetation as complex structures in fluid–filament interaction using the elastically-articulated body method. *Journal of Fluids and Structures*, **136**, 104323, https://doi.org/10.1016/j.jfluidstructs.2025.104323.

ECMWF,: Insurance impacts of European windstorms. Accessed 15 April 2024, https://stories.ecmwf.int/insurance-impacts-of-european-windstorms/.

Emeis, S., 2014: Current issues in wind energy meteorology. *Meteorological Applications*, **21**, 803–819, https://doi.org/10.1002/met.1472.

Featherstone, R., 1987: *Robot Dynamics Algorithms*. Springer US, https://doi.org/10.1007/978-0-387-74315-8.

Finnigan, J., 2000: Turbulence in Plant Canopies. *Annual Review of Fluid Mechanics*, **32**, 519–571, https://doi.org/10.1146/annurev.fluid.32.1.519.

Gardiner, B., P. Berry, and B. Moulia, 2016a: Review: Wind impacts on plant growth, mechanics and damage. *Plant Science*, **245**, 94–118, https://doi.org/10.1016/j.plantsci.2016.01.006.

——, ——, and ——, 2016b: Review: Wind impacts on plant growth, mechanics and damage. *Plant Science*, **245**, 94–118, https://doi.org/10.1016/j.plantsci.2016.01.006.

Gosselin, F. P., 2019: Mechanics of a Plant in Fluid Flow. *Journal of Experimental Botany*, **70**, 3533–3548, https://doi.org/10.1093/jxb/erz288.

Hadap, S., 2006: *Oriented Strands - Dynamics of Stiff Multi-Body System*. The Eurographics Association.

Hansen, K. S., R. J. Barthelmie, L. E. Jensen, and A. Sommer, 2012: The impact of turbulence intensity and atmospheric stability on power deficits due to wind turbine wakes at Horns Rev wind farm. *Wind Energy*, **15**, 183–196, https://doi.org/10.1002/we.512.

Hao, Y., G. A. Kopp, C.-H. Wu, and S. Gillmeier, 2020: A wind tunnel study of the aerodynamic characteristics of a scaled, aeroelastic, model tree. *Journal of Wind Engineering and Industrial Aerodynamics*, **197**, 104088, https://doi.org/10.1016/j.jweia.2019.104088.

Holmes, J. D., A. C. Allsop, and J. D. Ginger, 2014: Gust durations, gust factors and gust response factors in wind codes and standards. *Wind and Structures*, **19**, 339–352, https://doi.org/10.12989/was.2014.19.3.339.

IEC, 2005: *International Electrotechnical Commission, IEC 61400-1: Wind turbines – Part 1: Design requirements, 3rd ed., Geneva, Switzerland: IEC, 2005*.

Jackson, T., and Coauthors, 2019: Finite element analysis of trees in the wind based on terrestrial laser scanning data. *Agricultural and Forest Meteorology*, **265**, 137–144, https://doi.org/10.1016/j.agrformet.2018.11.014.

James, K. R., and B. Kane, 2008: Precision digital instruments to measure dynamic wind loads on trees during storms. *Agricultural and Forest Meteorology*, **148**, 1055–1061, https://doi.org/10.1016/j.agrformet.2008.02.003.

——, N. Haritos, and P. K. Ades, 2006: Mechanical stability of trees under dynamic loads. *American Journal of Botany*, **93**, 1522–1530, https://doi.org/10.3732/ajb.93.10.1522.

——, G. A. Dahle, J. Grabosky, B. Kane, and A. Detter, 2014: Tree Biomechanics Literature Review: Dynamics. *isa*, **40**, 1–15, https://doi.org/10.48044/jauf.2014.001.

Jiménez, P. A., E. García-Bustamante, J. F. González-Rouco, F. Valero, J. P. Montávez, and J. Navarro, 2008: Surface Wind Regionalization in Complex Terrain. *Journal of Applied Meteorology and Climatology*, **47**, 308–325, https://doi.org/10.1175/2007JAMC1483.1.

Klawa, M., and U. Ulbrich, 2003: A model for the estimation of storm losses and the identification of severe winter storms in Germany. *Natural Hazards and Earth System Sciences*, **3**, 725–732, https://doi.org/10.5194/nhess-3-725-2003.

Kulkarni, S., J. K. Hillier, T. I. Marjoribanks, S. L. Bugby, J. Higham, and D. Bannister, 2026: Seeing Gusty Winds: Optical Tracking of Tree Motion Captures Peak 3-s Gust Velocities. *Meteorological Applications*, **33**, e70156, https://doi.org/10.1002/met.70156.

Lombardo, F. T., 2021: History of the peak three-second gust. *Journal of Wind Engineering and Industrial Aerodynamics*, **208**, 104447, https://doi.org/10.1016/j.jweia.2020.104447.

Lv, N., J. Liu, H. Xia, J. Ma, and X. Yang, 2020: A review of techniques for modeling flexible cables. *Computer-Aided Design*, **122**, 102826, https://doi.org/10.1016/j.cad.2020.102826.

Met Office, 2023: Factsheet 6 - The Beaufort Scale, National Meteorological Library and Archive, Met Office.

Miller, L. A., 2005: Structural dynamics and resonance in plants with nonlinear stiffness. *Journal of Theoretical Biology*, **234**, 511–524, https://doi.org/10.1016/j.jtbi.2004.12.004.

Munson, B., D. Young, and T. Okiishi, 1998: Fundamentals of Fluid Mechanics. 3rd Edition, John Wiley & Sons, Inc., New York. Accessed 6 May 2026, https://www.wiley.com/en-us/Munson%2C+Young+and+Okiishi's+Fundamentals+of+Fluid+Mechanics%2C+8th+Edition-p-9781119547990R150.

Niklas, K. J., and H.-C. Spatz, 2000: Wind-induced stresses in cherry trees: evidence against the hypothesis of constant stress levels. *Trees*, **14**, 230–237, https://doi.org/10.1007/s004680050008.

Odijk, T., 2015: A tree swaying in a turbulent wind: a scaling analysis. *J Biol Phys*, **41**, 1–7, https://doi.org/10.1007/s10867-014-9361-0.

Ojo, O., and K. Shoele, 2022: Branching pattern of flexible trees for environmental load mitigation. *Bioinspir. Biomim.*, **17**, 056003, https://doi.org/10.1088/1748-3190/ac759e.

Pivato, D., S. Dupont, and Y. Brunet, 2014: A simple tree swaying model for forest motion in windstorm conditions. *Trees*, **28**, 281–293, https://doi.org/10.1007/s00468-013-0948-z.

Raupach, M. R., 1992: Drag and drag partition on rough surfaces. *Boundary-Layer Meteorol*, **60**, 375–395, https://doi.org/10.1007/BF00155203.

Ren, Z., M. Nikolopoulou, G. Mills, and F. Pilla, 2025: Evaluating the influence of urban trees and microclimate on residential energy consumption in Dublin neighbourhoods. *Building and Environment*, **269**, 112441, https://doi.org/10.1016/j.buildenv.2024.112441.

Roberts, J. F., and Coauthors, 2014: The XWS open access catalogue of extreme European windstorms from 1979 to 2012. *Natural Hazards and Earth System Sciences*, **14**, 2487–2501, https://doi.org/10.5194/nhess-14-2487-2014.

Rodriguez, M., E. de Langre, and B. Moulia, 2008: A scaling law for the effects of architecture and allometry on tree vibration modes suggests a biological tuning to modal compartmentalization. *American Journal of Botany*, **95**, 1523–1537, https://doi.org/10.3732/ajb.0800161.

Rodriguez, M., S. Ploquin, B. Moulia, and E. de Langre, 2012: The Multimodal Dynamics of a Walnut Tree: Experiments and Models. *J. Appl. Mech*, **79**, https://doi.org/10.1115/1.4005553.

Rudnicki, M., U. Silins, V. J. Lieffers, and G. Josi, 2001: Measure of simultaneous tree sways and estimation of crown interactions among a group of trees. *Trees*, **15**, 83–90, https://doi.org/10.1007/s004680000080.

Runia, T. F. H., K. Gavrilyuk, C. G. M. Snoek, and A. W. M. Smeulders, 2020: Cloth in the Wind: A Case Study of Physical Measurement Through Simulation. Proceedings of the IEEE/CVF Conference on Computer Vision and Pattern Recognition, 10498–10507.

Sellier, D., and T. Fourcaud, 2009: Crown structure and wood properties: Influence on tree sway and response to high winds. *American Journal of Botany*, **96**, 885–896, https://doi.org/10.3732/ajb.0800226.

——, ——, and P. Lac, 2006: A finite element model for investigating effects of aerial architecture on tree oscillations. *Tree physiology*, **26**, 799–806, https://doi.org/10.1093/treephys/26.6.799.

——, Y. Brunet, and T. Fourcaud, 2008: A numerical model of tree aerodynamic response to a turbulent airflow. *Forestry: An International Journal of Forest Research*, **81**, 279–297, https://doi.org/10.1093/forestry/cpn024.

Sevilla-Lara, L., D. Sun, E. G. Learned-Miller, and M. J. Black, 2014: Optical Flow Estimation with Channel Constancy. *Computer Vision – ECCV 2014*, D. Fleet, T. Pajdla, B. Schiele, and T. Tuytelaars, Eds, Cham, Springer International Publishing, 423–438, https://doi.org/10.1007/978-3-319-10590-1_28.

Simiu, E., and D. Yeo, 2019: *Wind Effects on Structures: Modern Structural Design for Wind. 4th edn. Hoboken, NJ: John Wiley & Sons.*

Spatz, H.-C., and F. Bruechert, 2000: Basic biomechanics of self-supporting plants: wind loads and gravitational loads on a Norway spruce tree. *Forest Ecology and Management*, **135**, 33–44, https://doi.org/10.1016/S0378-1127(00)00296-6.

Stull, R. B., 1988: *An Introduction to Boundary Layer Meteorology*.

Sun, D., S. Roth, and M. J. Black, 2014: A Quantitative Analysis of Current Practices in Optical Flow Estimation and the Principles Behind Them. *Int J Comput Vis*, **106**, 115–137, https://doi.org/10.1007/s11263-013-0644-x.

Suomi, I., and T. Vihma, 2018: Wind Gust Measurement Techniques—From Traditional Anemometry to New Possibilities. *Sensors (Basel)*, **18**, 1300, https://doi.org/10.3390/s18041300.

Tan, C., and W. Fang, 2018: Forest disturbance analysis with Landsat-8 OLI data related to a parametric wind field: A case study for Typhoon Rammasun (201409). Vol. 42 of, International Archives of the Photogrammetry, Remote Sensing and Spatial Information Sciences - ISPRS Archives, 1629–1633, https://doi.org/10.5194/isprs-archives-XLII-3-1629-2018.

Türk, M., and S. Emeis, 2010: The dependence of offshore turbulence intensity on wind speed. *Journal of Wind Engineering and Industrial Aerodynamics*, **98**, 466–471, https://doi.org/10.1016/j.jweia.2010.02.005.

Vogel, S., 1989: Drag and Reconfiguration of Broad Leaves in High Winds. *Journal of Experimental Botany - J EXP BOT*, **40**, 941–948, https://doi.org/10.1093/jxb/40.8.941.

Vogel, S., 1994: Life in Moving Fluids. The Physical Biology of Flow (Second Edition). Accessed 9 July 2026, https://www.scirp.org/reference/referencespapers?referenceid=2692069.

Wang, X., B. Chen, D. Sun, and Y. Wu, 2014: Study on Typhoon Characteristic Based on Bridge Health Monitoring System. *The Scientific World Journal*, **2014**, 204675, https://doi.org/10.1155/2014/204675.

Weber, J., J. E. Higham, J. Musser, and W. D. Fullmer, 2021a: Critical analysis of velocimetry methods for particulate flows from synthetic data. *Chemical Engineering Journal*, **415**, 129032, https://doi.org/10.1016/j.cej.2021.129032.

——, ——, ——, and ——, 2021b: Critical analysis of velocimetry methods for particulate flows from synthetic data. *Chemical Engineering Journal*, **415**, 129032, https://doi.org/10.1016/j.cej.2021.129032.

Zanotto, F., L. Marchi, and S. Grigolato, 2024: Wind-tree interaction: Technologies, measurement systems for tree motion studies and future trends. *Biosystems Engineering*, **237**, 128–141, https://doi.org/10.1016/j.biosystemseng.2023.12.005.

Zhang, Q., J. Xu, M. Crane, and C. Luo, 2022: See the wind: Wind scale estimation with optical flow and VisualWind dataset. *Science of The Total Environment*, **846**, 157204, https://doi.org/10.1016/j.scitotenv.2022.157204.

Zhou, W., A. Kasimu, Y. Wu, M. Tang, X. Liang, and C. Jiang, 2023: Wind Speed Measurement via Visual Recognition of Wind-Induced Waving Light Stick Target. *Applied Sciences*, **13**, 5375, https://doi.org/10.3390/app13095375.

Zille, P., T. Corpetti, L. Shao, and X. Chen, 2014: Observation Model Based on Scale Interactions for Optical Flow Estimation. *IEEE Transactions on Image Processing*, **23**, 3281–3293, https://doi.org/10.1109/TIP.2014.2328893.